

Coaxial Cable-Based Magnetic and Electric Near-Field Probes to Measure On-Chip Components up to 330 GHz

Benedikt Sievert¹, Member, IEEE, Jonathan Wittemeier², Member, IEEE, Jan Taro Svejda³, Member, IEEE, Nils Pohl⁴, Senior Member, IEEE, Daniel Erni⁵, Member, IEEE, and Andreas Rennings⁶, Member, IEEE

Abstract—This letter presents miniaturized near-field probes to characterize the electric and magnetic fields in the WR03 waveguide band (220–330 GHz) on-chip. The near-field probes are based on a commercially available coaxial cable, which enables the construction of both open- and short-circuited probes to measure electric and magnetic field components, respectively. Furthermore, it is flexible enough not to damage the wafer under test or the Ground-Signal-Ground (GSG) on-wafer probe contacting the chip. It is shown that the measured near fields enable physical insight into the operation of the chip, which also eases fault detection and the search for error sources. Finally, the electric and magnetic near fields measured above the chip can be used to calculate the far field of the chip antenna. Here, the usually disturbing influence of the on-wafer probe on the measurement can be significantly reduced if only the near field dominated by the antenna, i.e., in close proximity to the chip, is measured. With this technique, both probe radiation and shadowing can be mitigated. Compared with complex and accurate robot solutions necessary to measure the far field in spherical coordinates, the near-field measurement only requires a cartesian sampling along the chip surface.

Index Terms—Antenna measurements, coaxial components, millimeter (mm)-wave antennas, near-field measurement.

I. INTRODUCTION

MEASUREMENTS in the millimeter (mm)-wave on-chip environment are a challenging field of research since the decreasing sizes of devices and materials under test are characterized using electrically large waveguide flanges, on-wafer

probes, or even quasi-optical setups. For example, measurements of frontside-radiating on-chip antennas are usually limited due to the shadowing caused by the on-wafer probe [1]. Furthermore, the probe interferes with the radiation pattern of the antenna through its own radiation [2], [3] and the scattering of radiated fields at the probe body [4]. Especially for electrically large antennas, the near-field characterization of mm-wave antennas becomes more attractive as it enables both physical insight into the operation of the device under test and—with a reference measurement—even enables gain and efficiency calculations based on a near-to-far-field transform. Here, either aperture antennas in the near field [5], open-ended waveguide probes [6], [7], and fiber-optical-based E -field probes [8] are used to sample the field of interest. To minimize the probe footprint, and thus its influence on the measured field, and enable convenient on-wafer near-field probes, this letter introduces the use of coaxial cable-based near-field probes for the WR03-waveguide band (220–330 GHz). This coaxial cable is connected to a standard rectangular waveguide flange. It is thus usable with a vector network analyzer, a spectrum analyzer, or any other electronic- or photonic-based system using standardized waveguide flanges. It is acknowledged that using coaxial cable-based probes is not new in near-field measurements. For example, a method to calibrate the sensitivity of coaxial cable-based near-field probes up to 20 GHz is presented in [9]. Furthermore, a waveguide-to-coaxial-cable transition similar to the one presented here is given in [10], where an electric field probe operating up to 90 GHz is utilized to evaluate losses and different terminations of dielectric image lines. To the best of authors' knowledge, near-field probes based on coaxial cables have neither been presented in such a high-frequency band nor utilized for on-chip measurements.

The rest of this letter is organized as follows. Section II introduces the overall probe design for an electric- and magnetic near-field probe and the corresponding prototypes. Section III shows the near-field measurement and corresponding results for an on-chip antenna operating around 300 GHz. For comparison, finite-difference time domain (FDTD)-based full-wave simulation results are given here as well. Section IV presents the far field calculated from magnetic and electric near-fields and compares it with the full-wave simulation results. Here, the difference from conventional on-chip far-field measurements is discussed in detail. Finally, Section V concludes this letter.

Manuscript received 11 March 2023; revised 28 April 2023; accepted 27 June 2023. Date of publication 3 July 2023; date of current version 6 October 2023. This work was supported in part by the Deutsche Forschungsgemeinschaft (DFG, German Research Foundation) through projects C03 and C05 under Grant 287022738-TRR 196 MARIE and in part by the “terahertz.NRW,” through the Program “Netzwerke 2021,” an initiative of the Ministry of Culture and Science of the State of Northrhine Westphalia, under Grant NW21-068 C. We acknowledge support by the Open Access Publication Fund of the University of Duisburg-Essen. (Corresponding author: Benedikt Sievert.)

Benedikt Sievert, Jan Taro Svejda, Daniel Erni, and Andreas Rennings are with the General and Theoretical Electrical Engineering (ATE), University of Duisburg-Essen, CENIDE – Center for Nanointegration Duisburg-Essen, D-47048 Duisburg, Germany (e-mail: benedikt.sievert@uni-due.de; jan.svejda@uni-due.de; daniel.erni@uni-due.de; andre.rennings@uni-due.de).

Jonathan Wittemeier is with the Institute of Integrated Systems, Ruhr University, D-44801 Bochum, Germany (e-mail: jonathan.wittemeier@rub.de).

Nils Pohl is with the Institute of Integrated Systems, Ruhr University, D-44801 Bochum, Germany, and also with the Fraunhofer FHR, 53343 Wachtberg, Germany (e-mail: nils.pohl@rub.de).

Digital Object Identifier 10.1109/LAWP.2023.3291571

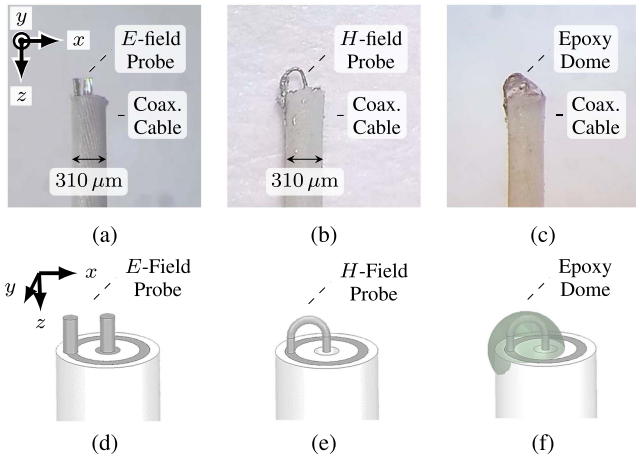


Fig. 1. Micrographs of (a) the fabricated E -field probe, (b) the B -field loop without, and with (c) the epoxy dome. The pursued probe geometry is depicted in (d) for the E -field probe without an epoxy dome and in (e) and (f) for the H -field probe without and with an epoxy dome.

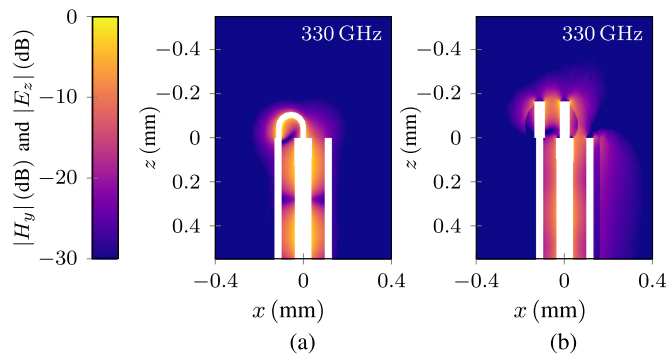


Fig. 2. (a) Simulated magnitude of the magnetic near-field at 330 GHz for the H -field probe. (b) Magnitude of the electric near-field for the E -field probe. Simulations have been carried out using Ansys HFSS.

II. PROBE DESIGN

The probe is based on the Alpha Wire 9442 with an outer diameter of $\approx 310 \mu\text{m}$, which enables mono-mode operation within the WR03 waveguide band. All dimensions are based on the manufacturer's datasheet [11]. The inner conductor consists of seven stranded wires with a total diameter of $76 \mu\text{m}$, and the outer conductor starts at $196 \mu\text{m}$. Two different sensor types are used, namely, an open-circuited parallel wire to measure the E_x component and a closed loop to measure the B_y component. The corresponding coordinate system used in this letter is given, along with simulation screenshots and micrographs of the prototypes in Fig. 1. All prototypes are manually cut, and in the case of the loop, bent, and soldered by hand. Within the limitations of accuracy, we have tried to manufacture the simulated geometries as well as possible. Although only shown for the loop in Fig. 1(c), the electric field probe with the two parallel wires has also been sealed using epoxy glue. The simulation considers the epoxy glue as a spherical dome of relative permittivity $\epsilon_{r, \text{epoxy}} = 2.9$, and a loss tangent of $\tan \delta = 0.02$. The simulated electric and magnetic near-fields caused by the respective probe are shown in Fig. 2 for the upper band limit of the WR03 waveguide band, i.e., 330 GHz. It can be seen that the loop size is chosen to achieve a maximum magnetic field strength at the center of the loop. In

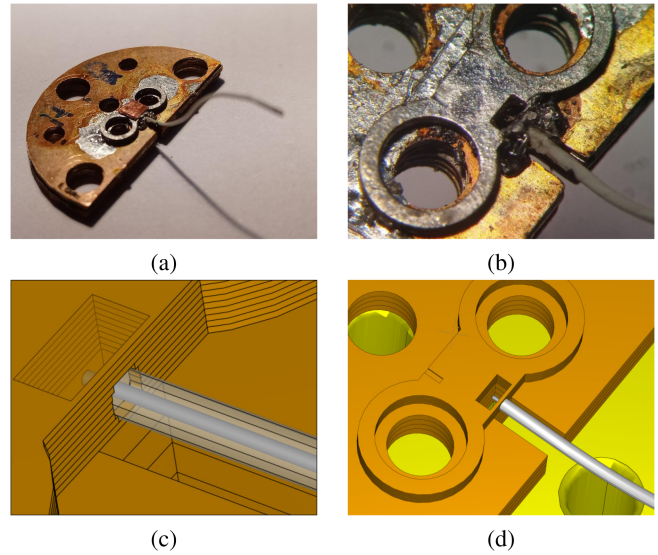


Fig. 3. Probe to waveguide transition (a) in perspective view on the soldered prototype and (b) detailed view on the cable collet, as well as (c) stacked CAD model, and (d) the CAD-assembled transition. In (b), the waveguide short circuit built by a final copper layer is not yet applied, such that the inner conductor of the coaxial cable can be seen.

contrast, the open circuit naturally produces a large electric field between the parallel wires.

The transition from coaxial cable to rectangular waveguide uses the well-known $\approx \lambda/4$ distance between the feed point and waveguide short circuit, and the inner conductor of the coaxial cable excites the fundamental TE_{10} mode in the rectangular waveguide (cf. Fig. 3). Although the length of the feeding inner conductor has been optimized to obtain better impedance matching, the performance limitation is here dominated by the accuracy of manufacturing the prototypes. For assembly without micro-machining, the waveguide-to-coaxial transition is realized with an approach similar to the split-block technique using a stack of considerably shaped copper-beryllium sheets of $50 \mu\text{m}$ and $250 \mu\text{m}$ thickness (cf., Fig. 3). The thicker $250 \mu\text{m}$ sheets are designed to match the UG387/U flange, whereas the thinner $50 \mu\text{m}$ sheets build a collet for the coaxial cable if assembled in the correct order [cf., Fig. 3(c)]. Photographs of the waveguide-to-coax transition and the simulation model for comparison are given in Fig. 3(b) and (d). Here, the short circuit at the end of the waveguide has been temporarily removed to enable the observation of the correct coaxial probe position.

III. PROBE MEASUREMENTS ON CHIP

To show the feasibility of the on-wafer measurement using the coaxial cable near-field probe, a linear polarized on-chip antenna consisting of four radiating dipoles is characterized. Details on the antenna and the operation principle can be found in [12]. The antenna is fed using a commercial GSG on-wafer probe and the R&S ZC330 frequency extender. The coaxial probe is connected via a rectangular waveguide to an R&S ZRX330 receiver on a motorized x - y - z -stage. With a straightforward transmission measurement, the magnetic or electric near-fields are measured by meandering the coaxial probe over the chip surface, i.e., scanning the x - y or x - z -plane. A micrograph of the

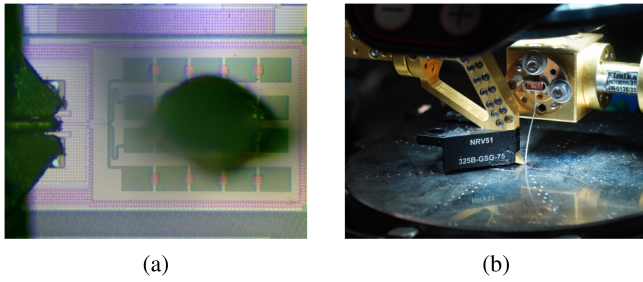


Fig. 4. Micrograph of (a) the investigated chip-antenna with the coaxial probe hovering over the antenna and (b) photograph of the chip-antenna on the chuck with the on-wafer GSG probe and the coaxial magnetic field probe.

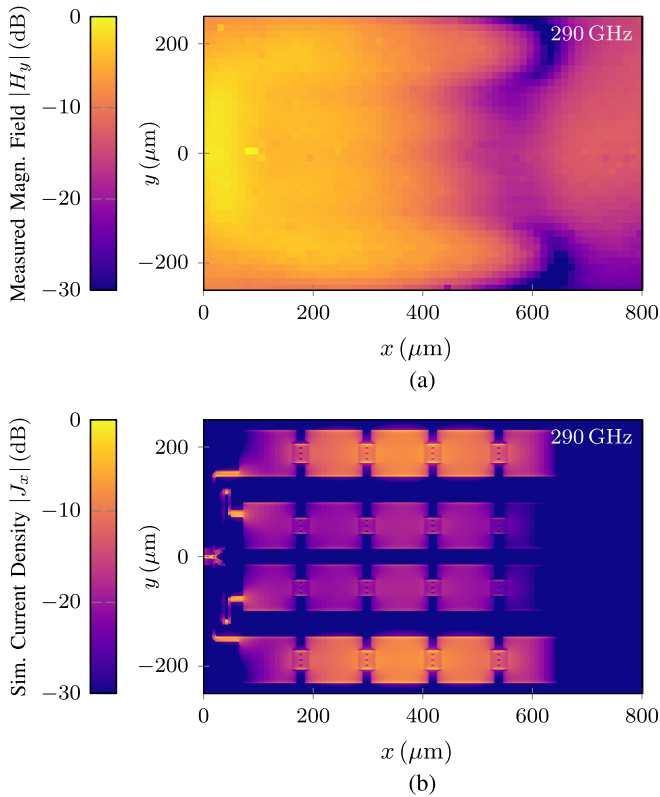


Fig. 5. Magnitude of (a) the measured magnetic field strength y -component H_y on the chip surface and (b) the corresponding FDTD-simulated current density x -component J_x in all metal layers at 290 GHz.

antenna and a photograph of the chip with GSG and coaxial probe in contact are depicted in Fig. 4. It should be noted that the coaxial cable is sufficiently rigid to be moved without further mechanical support on the chip area. However, both a collision with the chip surface indicating a wrong coaxial probe height and a collision with the on-wafer probe can be recognized with the microscope as a bending motion of the cable. This enables a straightforward assessment of the correct measurement height—the coaxial probe is lowered until it touches the wafer and then lifted by a few μm to hover over the chip area. The collision with the GSG on-wafer probe is also harmless, as the coaxial cable is highly flexible compared with the GSG probe.

As abovementioned, the antenna under test consists of four dipoles, from which each two are resonant at the same frequency. At ≈ 290 GHz, Fig. 5(a) shows the magnetic field's y -component measured at the chip surface using the loop probe.

For comparison, the simulated current density in the x -direction J_x is shown in Fig. 5(b). The simulation has been carried out using Empire XPU, and the current density displayed is an overlay of the current densities in all underlying metal layers. For the measurement, a step size of $\Delta x = \Delta y = 12.5 \mu\text{m}$ has been chosen, and the measured field quantity is depicted without any interpolation method. Although the measured magnetic near-field is blurred by both the finite probe footprint and the near-field measurement height above the chip surface, the correct operation of the antenna is clearly visible. This underlines how coaxial mm-wave near-field probes enable physical insight or fault detection.

IV. FAR-FIELD CALCULATION FROM MEASURED NEAR-FIELDS

Measuring the antenna radiation pattern of typical on-chip antennas is challenging for several reasons [3], [13]. First, the typically utilized robotic systems to sample the antenna radiation are expensive, bulky, and limited in position accuracy [14]. For phase-correct measurements with multiaxis robots, position feedback, and correction require implementation effort but yield excellent results [5]. Tailored two- or three-axis robots using spherical coordinates are, however, less flexible in their applicability, although they offer inherently good measurement performance [15], [16], [17]. Second, the on-wafer probe has a severe effect on the measured radiation pattern for all frontside radiating antennas. This is caused by the radiation of the probe itself [2], [3], scattering of radiated waves at the probe [4], and shadowing of the radiated fields [18]. The near-field measurements presented in the following can mostly circumvent these effects since it requires only a cartesian sampling of the near field over the chip area and since the measured near-fields are strongly dominated by the on-chip antenna. It should be noted that the measurement is carried out in the reactive near-field, which features comparably high field strengths. Furthermore, the electric and magnetic field strength are measured to calculate the resulting far-field based on equivalent magnetic and electric current densities according to Love's principle [19, p. 655] without the necessity of using any method of images. For all measurements, the VNA was set up to acquire 22 frequency points between 220 and 330 GHz with a measurement bandwidth of 1 kHz to enable a quick acquisition, where each cut plane took about min to evaluate the near-field sampling points. The measured antenna geometry is schematically depicted with the utilized coordinate system in Fig. 6(a). The vertical cut planes at $y = 0$ in Fig. 6(b) and (c) shows the instantaneous electric and magnetic field strength in the x - and y -components at GHz, respectively, which has been measured in coarser steps of $\Delta x = \Delta z = 25 \mu\text{m}$. The corresponding horizontal cuts at $z = 0$ are depicted in Fig. 6(d) and (e), where a finer grid of $\Delta x = \Delta y = 12.5 \mu\text{m}$ was chosen for an accurate near-to-far-field transform. To compare the intensity of both field strengths, the measured near-fields at $z = 1$ mm are compared with magnitude and phase. It is expected that the ratio between orthogonal magnetic and electric field strength approaches η_0 , and a complex scaling factor K has been chosen to fulfill

$$K E_z(z = 1 \text{ mm}) = \eta_0 H_y(z = 1 \text{ mm}). \quad (1)$$

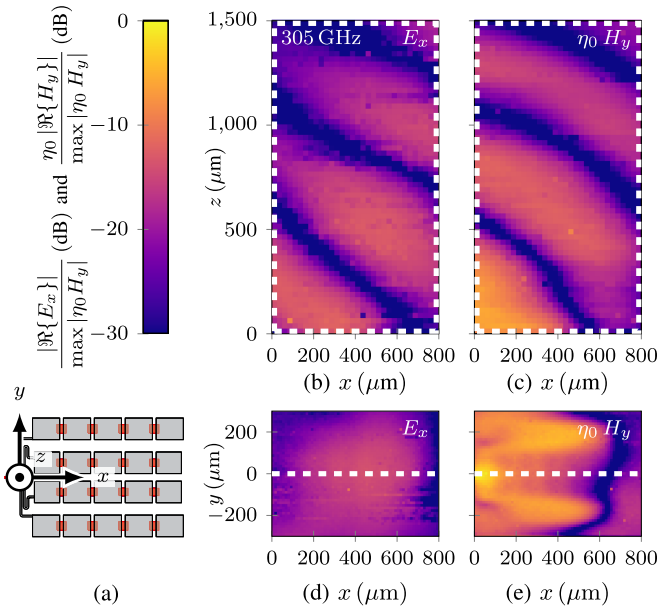


Fig. 6. Schematic top view on the investigated on-chip antenna with (a) the utilized coordinate system, the instantaneous field in the measured vertical cut ($y = 0$) of (b) E_x and (c) H_y , and (d) the measured horizontal cut ($z = 0$) of E_x and (e) H_y at 305 GHz. Since the instantaneous field is shown, the phase fronts of the radiated waves can be identified.

The accuracy of this normalization depends on the utilized distance between the antenna and the measurement point, where close proximity to the antenna would imply nonorthogonal and possibly phase-shifted field components. This factor is applied to all measured electric field strengths, such that electric and magnetic field quantities can be normalized to $\max |\eta_0 H_y|$ in Fig. 6. With this normalization, the magnetic field strength dominates the horizontal cut plane [cf., Fig. 6(d) and (e)] close to the antenna. Especially in the vertical cut plane of the E_z component, the measured field quantity exhibits larger noise contributions. This is caused by the (lower) sensitivity of the electric field probe, which resulted in a factor $|K \eta_0| \approx 423 \text{ V/A}$ to upscale the electric field with respect to the magnetic field. Furthermore, the radiation in the vertical cut planes is probably superimposed with the field radiated from the on-wafer probe.

To minimize this probe influence, the near-to-far-field transform is carried out with data obtained in close proximity to the chip surface. The equivalent magnetic and electric current densities have been assigned using the fields of the horizontal cut from Fig. 6(d) and (e), and the equivalent currents outside the measured range are assumed zero. To consider the probe sensitivity and possibly different electrical lengths of the coaxial cables for E and H field probes, the correction factor K from (1) is used to weigh the magnetic currents. With this normalization, the radiated far field can be calculated qualitatively, and two cut planes normalized to the maximum directivity are depicted in Fig. 7. For a quantitative gain calculation, the near-field of a well-known reference antenna needs to be measured, as shown in [7]. With the antenna gain data and directivity normalization, even the overall antenna efficiency could be calculated [7], which is challenging for far-field measurements with the influence of

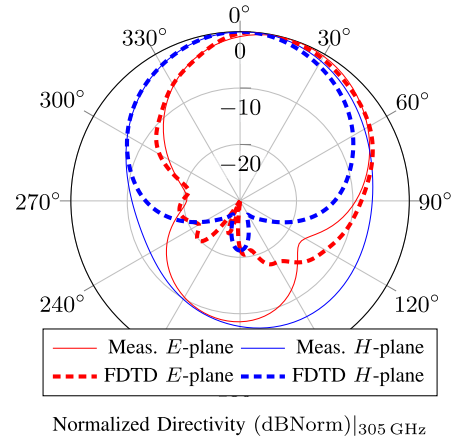


Fig. 7. Radiation pattern calculated from the near-fields in Fig. 6(d) and (e) and compared with the FDTD full-wave simulation result (Empire XPU) normalized to the maximum value at 305 GHz.

an on-wafer probe [1]. For comparison, the antenna's far-field calculated with the full-wave FDTD solver is given as well, and the agreement is excellent in the forward direction. A precise description of the backward radiation ($90^\circ \leq \theta \leq 270^\circ$) is expected if the measured region of the near-field is increased. The radiation patterns show a better agreement in the E -plane (the x - z -plane), which is caused by the increased measurement range along the x -axis ($800 \mu\text{m}$) compared with the y -axis range ($500 \mu\text{m}$). Overall, the agreement is very good, especially given the stunning simplicity of the measurement method. Observe that the noise in the measured near fields has a minor effect on the far fields, as the near-to-far-field transform involves surface integrals that average the noise contributions. In contrast, the far field measurement of the same antenna presented in [12] shows the typical issues associated with on-wafer far-field measurements, such as undulations in the measured pattern due to interference with probe radiation or the probe scattering and shadowing in the far field region.

V. CONCLUSION

This letter has presented coaxial cable-based near-field probe sensors operating between 220 and 330 GHz. The sensors are designed to receive dominantly magnetic or electric fields by using nonideal open or short circuits, respectively. Using a transition to a standardized rectangular waveguide, the sensors can be applied with any measurement device using the WR03 waveguide, such as frequency converters, mixers and power detectors. Furthermore, the mechanical flexibility of the cable enables nondestructive measurement of magnetic and electric fields close to the chip surface. Besides the physical insight that can be generated with this method, it might become useful for on-chip fault detection and has been shown to enable a straight-forward far-field calculation of on-chip antennas. It has been demonstrated that the influence of the probe tip can effectively be reduced such that the limiting effects of on-wafer probes on on-chip measurements, i.e., shadowing, scattering, and probe radiation, are mitigated.

REFERENCES

- [1] D. Titz, F. Ferrero, P. Brachat, G. Jacquemod, and C. Luxey, "Efficiency measurement of probe-fed antennas operating at millimeter-wave frequencies," *IEEE Antennas Wireless Propag. Lett.*, vol. 11, pp. 1194–1197, 2012.
- [2] K. Mohammadpour-Aghdam, S. Brebels, A. Enayati, R. Faraji-Dana, G. A. E. Vandenbosch, and W. DeRaedt, "RF probe influence study in millimeter-wave antenna pattern measurements," *Int. J. RF Microw. Comput.-Aided Eng.*, vol. 21, no. 4, pp. 413–420, 2011.
- [3] H. Zhang and A. Shamim, "Tackling the issues of millimeter-wave on-chip antenna measurements," in *Proc. 13th Eur. Conf. Antennas Propag.*, 2019, pp. 1–5.
- [4] L. Boehm, M. Hitzler, F. Roos, and C. Waldschmidt, "Probe influence on integrated antenna measurements at frequencies above 100 GHz," in *Proc. 46th Eur. Microw. Conf.*, 2016, pp. 552–555.
- [5] J. A. Gordon et al., "Millimeter-wave near-field measurements using coordinated robotics," *IEEE Trans. Antennas Propag.*, vol. 63, no. 12, pp. 5351–5362, Dec. 2015.
- [6] Z.-M. Tsai, Y.-C. Wu, S.-Y. Chen, T. Lee, and H. Wang, "A V-band on-wafer near-field antenna measurement system using an IC probe station," *IEEE Trans. Antennas Propag.*, vol. 61, no. 4, pp. 2058–2067, Apr. 2013.
- [7] A. Jam and K. Sarabandi, "A submillimeter-wave near-field measurement setup for on-wafer pattern and gain characterization of antennas and arrays," *IEEE Trans. Instrum. Meas.*, vol. 66, no. 4, pp. 802–811, Apr. 2017.
- [8] Y. Tanaka et al., "Photonics-based near-field measurement and far-field characterization for 300-GHz band antenna testing," *IEEE Open J. Antennas Propag.*, vol. 3, pp. 24–31, 2022.
- [9] Y. Gao, A. Lauer, Q. Ren, and I. Wolff, "Calibration of electric coaxial near-field probes and applications," *IEEE Trans. Microw. Theory Techn.*, vol. 46, no. 11, pp. 1694–1703, Nov. 1998.
- [10] K. Solbach, "Electric probe measurements on dielectric image lines in the frequency range of 26–90 GHz," *IEEE Trans. Microw. Theory Techn.*, vol. MTT-26, no. 10, pp. 755–758, Oct. 1978.
- [11] Alpha Wire, "Coaxial cable 9442." Accessed: Apr. 28, 2023. [Online]. Available <https://www.alphawire.com/Products/cable/alpha-essentials/coaxial-cable/9442>
- [12] B. Sievert, J. T. Svejda, J. Wittemeier, N. Pohl, D. Erni, and A. Rennings, "Equivalent circuit model separating dissipative and radiative losses for the systematic design of efficient microstrip-based on-chip antennas," *IEEE Trans. Microw. Theory Techn.*, vol. 69, no. 2, pp. 1282–1294, Feb. 2021.
- [13] H. Gulan, C. Luxey, and D. Titz, "mm-Wave sub-mm-wave antenna measurement," in *Handbook of Antenna Technologies*, Z. N. Chen, D. Liu, H. Nakano, X. Qing, and T. Zwick, Eds. Singapore: Springer, 2016, pp. 2191–2238.
- [14] D. J. van Rensburg and S. F. Gregson, "Parametric study of probe positioning errors in articulated spherical near-field test systems for mm-wave applications," in *Proc. 2014 IEEE Conf. Antenna Meas. Appl.*, 2014, pp. 1–4.
- [15] J. Akkermans, R. van Dijk, and M. Herben, "Millimeter-wave antenna measurement," in *Proc. Eur. Microw. Conf.*, 2007, pp. 83–86.
- [16] S. Beer and T. Zwick, "Probe based radiation pattern measurements for highly integrated millimeter-wave antennas," in *Proc. 4th Eur. Conf. Antennas Propag.*, 2010, pp. 1–5.
- [17] B. Sievert, J. T. Svejda, D. Erni, and A. Rennings, "Spherical mm-Wave/THz antenna measurement system," *IEEE Access*, vol. 8, pp. 89680–89691, 2020.
- [18] D. Titz, F. Ferrero, and C. Luxey, "Development of a millimeter-wave measurement setup and dedicated techniques to characterize the matching and radiation performance of probe-fed antennas," *IEEE Antennas Propag. Mag.*, vol. 54, no. 4, pp. 188–203, Aug. 2012.
- [19] C. A. Balanis, *Antenna Theory: Analysis and Design*, 3rd ed. Hoboken, NJ, USA: Wiley, 2005.